Diffusive and Drift Halide Perovskite Memristive Barristors as Nociceptive and Synaptic emulators for Neuromorphic Computing

Rohit Abraham John[1#], Natalia Yantara[2#], Si En Ng[1], Muhammad Iszaki Bin Patdillah[2], Mohit Rameshchandra Kulkarni[1], Nur Fadilah Jamaludin[2], Joydeep Basu[3], Ankit[1], Subodh G. Mhaisalkar[1,2], Arindam Basu[3], Nripan Mathews[1,2]**

[1] School of Materials Science and Engineering, Nanyang Technological University, 50 Nanyang Avenue, Singapore 639798

[2] Energy Research Institute @ NTU (ERI@N), Nanyang Technological University, Singapore 637553

[3] School of Electrical and Electronic Engineering, Nanyang Technological University, 50 Nanyang Avenue, Singapore 639798

[#]These authors contributed equally to this work

* Corresponding authors

Prof. Arindam Basu (Email: arindam.basu@ntu.edu.sg)

Prof. Nripan Mathews (Email: nripan@ntu.edu.sg)

Keywords: diffusive memristor, drift memristor, halide perovskite barristor, neuromorphic computing, artificial nociceptor

Abstract

With the current research impetus on neuromorphic computing hardware, realizing efficient drift and diffusive memristors are considered critical milestones for the implementation of readout layers, selectors and frameworks in deep learning and reservoir computing networks. Current demonstrations are predominantly limited to oxide insulators with a soft breakdown behaviour. While organic ionotronic electrochemical materials offer an attractive alternative, their implementations thus far have been limited to features exploiting ionic drift a.k.a. drift memristor technology. Development of diffusive memristors with organic electrochemical materials is still at an early stage and modulation of their switching dynamics remains unexplored. Here we propose and experimentally demonstrate halide perovskite memristive barristors (diodes with variable Schottky barriers) portraying tunable diffusive dynamics and ionic drift for the first time. We identify an ion permissive poly(3,4-ethylenedioxythiophene) polystyrene sulfonate (PEDOT:PSS) interface that promotes diffusive kinetics and an ion source nickel oxide (NiO_x) interface that supports drift kinetics to design diffusive and drift memristors respectively with methylammonuim lead bromide ($CH_3NH_3PbBr_3$) as the switching matrix. In line with the recent interest on developing artificial afferent nerves as information channels bridging sensors and artificial neural networks, we fashion these halide perovskite memristive barristors as nociceptive and synaptic emulators for neuromorphic sensory signal computing.

Introduction

With the increasing need for rapid data shuttling between physically-separate memory and processing units, classical computing architectures are constantly challenged by the heat, memory and scaling walls, particularly for data-centric applications such as artificial intelligence and machine learning[1]. With the natural co-location of memory and compute in the same device, memristor technology eliminates this need for constant data movement, and provides a more-efficient alternative for bioinspired in-memory computing[2,3]. Recently, tunable organic ionotronic (ionic+electronic) electrochemical materials have garnered significant interests to build biorealistic memristors in light of their ability to possess basic forms of neuroplasticity that can emulate brain-like functionality (e.g. slow time-scale dynamics due to calcium ions) without additional circuitry[4–6]. In comparison to the manipulation of atomic defects in inorganic materials, the large number of state variables or physical degrees of freedom available in ionotronic systems and the ability to directly tune the material characteristics such as redox states, allow these materials to be used as building blocks for efficient "scaled-in" neuromorphic architectures[7,8]. This concept of "scaling-in"- to boost the information space per cell without escalating the material and area budget, bears close resemblance to biological neural networks and is a crucial approach towards realizing a practical system.

While efforts to intimately integrate complementary metal-oxide-semiconductor (CMOS) electronics with memristors continue to be the most straightforward approach to improve the energy efficiency and speed

of the system, attempts to realize an all-memristive computing platform has recently resulted in the discovery of two major classes of memristors- drift and diffusive[9]. While drift memristors are expected to cater to the requirements of precise multi-bit non-volatile weight updates and readout layers, diffusive memristors are anticipated to play vital roles as non-linear selectors and frameworks for deep learning networks and reservoir computing respectively[5,10,11]. More interestingly, diffusive memristors have been very recently employed as artificial nociceptors[12] to filter noxious information from sensing elements, expanding the research portfolio of memristor technology and in-memory computing to new horizons of intelligent sensory systems and robotics[13]. While impressive progress has been made in this context with metal oxide based memristors, ionotronic materials that display a close coupling of ionic motion and electronic conduction have not been investigated systematically for building diffusive memristors[14,15]. Most of the research on ionotronic materials have thus far been limited to drift memristor technology based on ionic drift that enables non-volatile weight updates for spiking or deep neural networks. Diffusive memristor technology with biologically plausible Ca^{2+} dynamics[10] is still at their germinal stage, hence presenting a need to explore new ionotronic materials to design efficient diffusive memristors.

Ionotronic materials with unique short-term memory properties would enable facile demonstration of threshold switching physics and could play a vital role in this regard. Recently, ionotronic halide perovskite (HP) semiconductors possessing exotic optoelectronic properties such as mixed ionic and electronic conduction, switchable majority carrier concentration and slow photocurrent decay have been demonstrated as a promising material set to design the next generation of neuromorphic memristors[16–18]. While electrochemical metallization reactions with reactive electrodes have been widely exploited to design digital/binary memristors, vacancy-driven ion migration and modulation of injection barriers at perovskite-transport layer interfaces have been utilized to realize analog memristors and artificial synapses[19–24]. Despite impressive progress with lower dimensional and lead-free perovskites, the specific influence of interfacial injection layers and the intrinsic doping within the perovskite layers have not been rationally studied yet[25]. Intuitively, the transport characteristics of such memristors will be majorly determined by the electronic properties of these functional interfaces, and hence entails systematic investigation to realize memristive devices with tunable drift and diffusive dynamics.

Identifying interfaces as a critical determinant in defining the switching dynamics of HP memristors, here we propose two key interfaces- an ion permissive poly(3,4-ethylenedioxythiophene) polystyrene sulfonate (PEDOT:PSS) interface that promotes diffusive kinetics and an ion source nickel oxide (NiO_x) interface that supports drift kinetics to design diffusive and drift memristors respectively with methylammonium lead bromide ($CH_3NH_3PbBr_3$) as the active switching matrix. Extending this concept, we design the first diffusive and drift memristive barristors (diodes with variable Schottky barriers) based on halide perovskites (HP) for neuromorphic computing. We begin with comprehensively characterizing the

switching characteristics of both configurations and investigating the underlying switching physics (Figs. 1-2). As an application benchmark, we configure our diffusive and drift memristive barristors as artificial nociceptors (Figs. 3-4) and synapses (Fig. 5) and comprehensively investigate their neuromorphic characteristics. We report the first diffusive halide perovskite memristor and artificial nociceptor to the best of our knowledge. We also present the first comprehensive analysis of the soft boundaries of conductance updates in perovskite artificial synapses - crucial for neuromorphic circuitry. Finally, we integrate these elements on to a sensorized robotic arm and demonstrate a prototypical sensory signal computing platform that learns noxious sensory information and trigger reflex reactions for intelligent robotics (Fig. 6). The prototypical memristive sensory signal processing platform composed of artificial perovskite nociceptors, synapses and CMOS neurons, although simple, is the first of its kind, serves as a proof-of-concept illustration and represents a significant advance over existing artificial nociceptor and afferent nerve implementations.

Results

Designing Diffusive and Drift Halide Perovskite Memristive Barristors

To design diffusive and drift halide perovskite barristors, here we utilize methylammonium lead bromide ($MAPbBr_3$) with established ionic-electronic properties as the memristive active material template[16]. Anti-solvent assisted spin coating method was used to deposit compact the $MAPbBr_3$ films. X-Ray Diffraction (XRD) patterns indicate that the resulting $MAPbBr_3$ films belong to Pm3m space group with a lattice constant of 5.927Å, in agreement with previous reports[26]. Crystallite size of ~ 50 nm is obtained from the Scherrer equation and a preferred growth in the <100> plane is observed (Supplementary Note 1, Supplementary Figure 1). The optical bandgap of the material is approximately 2.3 eV, determined from both photoluminescence (PL) and absorbance spectra (Supplementary Note 1, Supplementary Figure 1). As excitonic resonance dominates at the absorption onset, Elliott's formula is used to decouple both excitonic and continuum contributions[27]. The small Stokes shift between PL and absorbance spectra indicates direct band-to-band radiative recombination nature of the system.

The memristors are fabricated by sandwiching $MAPbBr_3$ in between hole (HTL) and electron transporting layers (ETL) connected to indium tin oxide (ITO) and aluminium (Al) electrodes respectively. While 1,3,5-triazine-2,4,6-triyl)tris(benzene-3,1-diyl)tris(diphenylphosphine oxide) (PO-T2T) serves as the ETL, two types of HTL are employed, i.e. poly(3,4-ethylenedioxythiophene) polystyrene sulfonate (PEDOT:PSS) and nickel oxide (NiO_x), to create diffusive and drift memristors respectively. NiO_x is hypothesized to act as an interlayer promoting drift kinetics via defect-assisted filament formation across the perovskite/NiO_x interface while the ion permissive PEDOT:PSS/perovskite interface is chosen to build memristors with diffusive kinetics. Similar HTL and ETL thickness are deployed in both diffusive and drift memristors (Fig. 1a). Despite identical deposition conditions, a slightly thicker $MAPbBr_3$ film formation is observed when

PEDOT:PSS (250 nm) is employed as the substrate as compared to NiO_x (220 nm). The difference in the wetting properties between PEDOT:PSS and NiO_x might be responsible for the thickness variation.

Under mild bias application (up to 3 V), higher currents (I) are observed in the reverse scan direction as compared to forward direction for both PEDOT:PSS and NiO_x devices (Fig. 1b). These current hystereses could be attributed to the migration of ions inside the perovskite films which have been observed widely[28–31]. Under forward bias application, negative ions and vacancies (i.e. Br^-, V_{MA}^-) aggregate and accumulate at the HP-HTL interface to create a self p-type doped region while a self n-doped region is formed at the HP-ETL interface due to accumulation of positive ions and vacancies (i.e. V_{Br}^+, MA^+) (Accumulation, Fig. 1c). The self-doping mechanism (intrinsic formation of p- and n-rich regions) at the perovskite-TL interfaces improve the carrier injection (decreases the barrier) to the perovskite, resulting in a higher current flow. Larger current hysteresis is observed for PEDOT:PSS devices in this voltage range (0-3 V). This is ascribed to the higher initial hole injection barrier from PEDOT:PSS to the perovskite layer, as observed from both the band diagram constructed after UPS measurement and higher photoluminescence (PL) quenching of perovskite films with the PEDOT:PSS interface indicating either greater hole flow to the TL and/or higher interfacial defects in the system (Supplementary Note 1, Supplementary Figure 2). Despite the current hysteresis, the initial current is recovered upon removing the external bias as ions diffuse back, thus portraying a diffusive volatile threshold behaviour for both PEDOT:PSS and NiO_x devices under mild bias.

Upon sweeping to higher bias (6V), the NiO_x devices depict a typical bipolar drift non-volatile memristive behaviour switching from a high resistance state (HRS) to a low resistance state (LRS) with positive bias application (SET) and vice versa for negative bias application (RESET). On the other hand, the PEDOT:PSS devices continue to portray a volatile diffusive memristor behaviour even up to 8 V (Fig. 1b). The non-volatile behaviour of the NiO_x devices can be attributed to its ability to support conductive filament formation in the device via ion migration. At higher positive bias the negative and positive ions drift and aggregate further, evolving into a conductive filament which acts as a shunt path lowering the device's resistance (SET, Fig. 1c). In halide perovskites, these filaments are most likely formed by halogen vacancies[32]. Electrochemical reaction between NiO_x and halide perovskite upon electrical bias[33], and halide oxidation promoted by NiO_x[34] might further increase halogen vacancies in the system and increase the probability of conductive filament formation. Upon sufficient negative bias application, the ions drift to the opposite direction rupturing the conductive filament and subsequently increases the device's resistance (RESET, Fig. 1c).

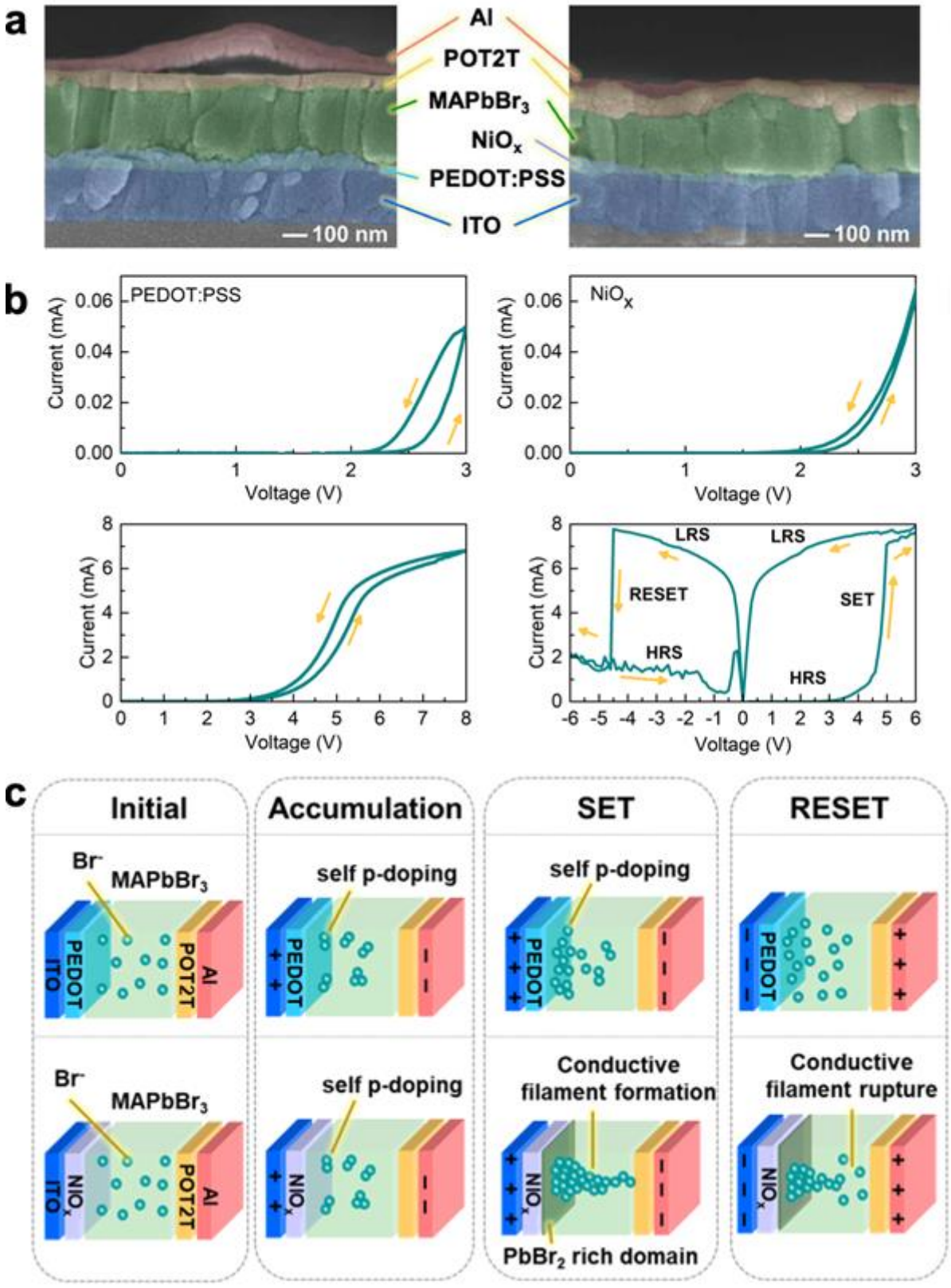

Fig 1. Designing Diffusive and Drift Halide Perovskite (HP) Memristive Barristors. a Cross sectional SEM images of the diffusive and drift memristor structures with PEDOT:PSS and NiO_x HTLs. **b** Current voltage (I-V) sweep characteristics of the memristive barristors depicting diffusive and drift kinetics. **Memristor mechanism. c** The proposed memristive mechanism of HP barristors with PEDOT:PSS and NiO_x as the HTLs.

To gather insight into how the HTL interfaces affect the memristive mechanism of halide perovskite barristors, secondary electron imaging (SEI) and backscattered electron imaging (LABE) experiments are conducted on both PEDOT:PSS and NiO_x devices before and after bias application (~ 8 V). The electron microscopy images reveal similar morphology and thickness for both devices and no changes to these features upon bias application. Interestingly, the LABE images indicate the growth of white domains (high density materials) starting at the HTL/perovskite interface for the NiO_x devices after bias application (Fig. 2 and Supplementary Figure 3). This is attributed to $PbBr_2$ rich perovskite domains as explained below.

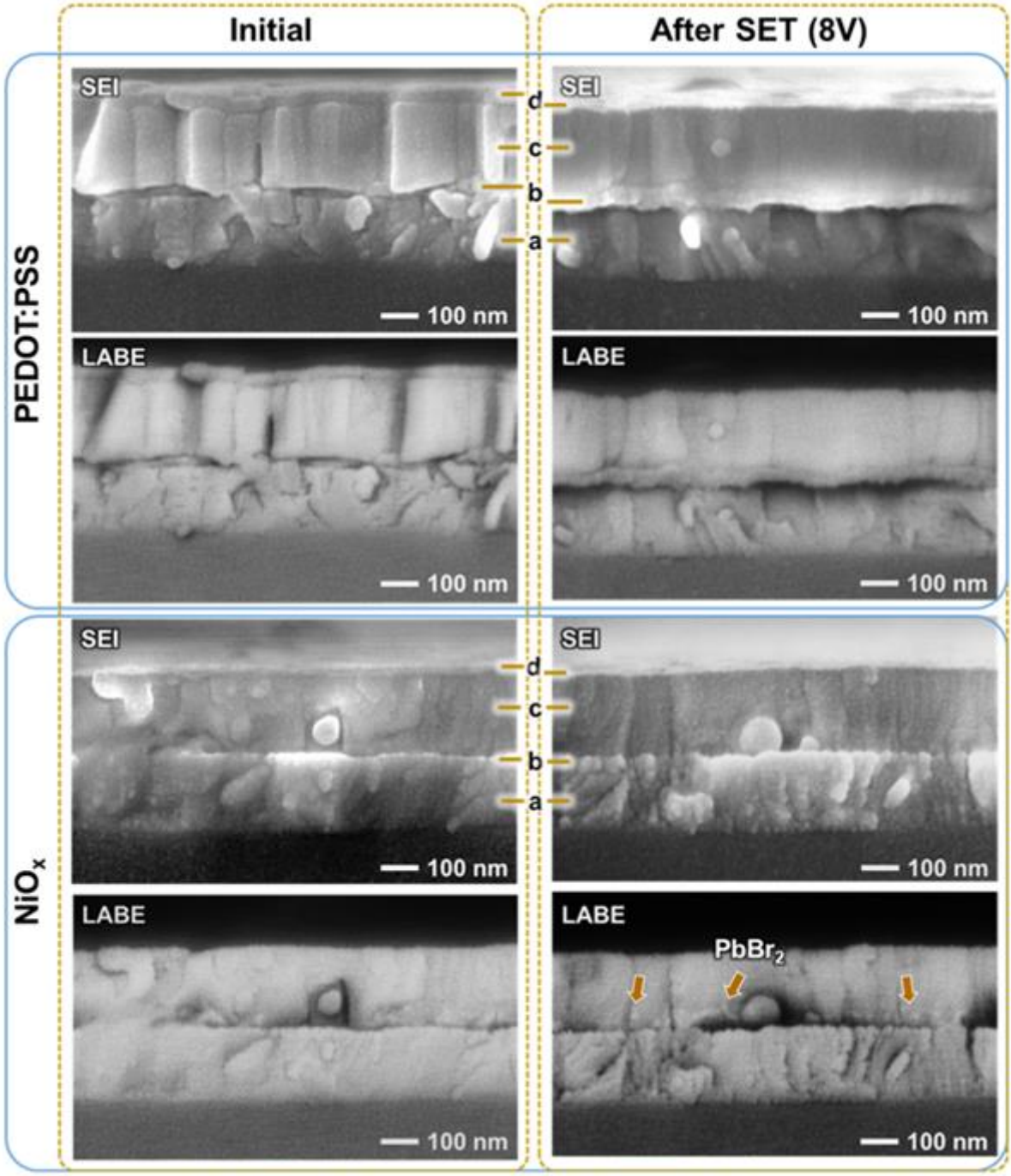

Fig 2. Evidence for interfacial reactions. The secondary electron image (SEI) and backscattered electron image (LABE) of PEDOT:PSS and NiO_x-based devices before and after bias application (8 V). Note: a, b, c, and d correspond to ITO, HTL, $MAPbBr_3$, and ETL layers respectively.

Temperature-accelerated studies are further performed to study the evolution of this reaction at the HTL/perovskite interface. The HTL/perovskite substrates are first heated at various temperatures (100°C refer to as deposited, 120°C, and 150°C) for 20 minutes. X-Ray Diffraction (XRD) spectroscopy is initially conducted on the substrates with a high incident angle (10°) to collect signals from the buried interface (Supplementary Fig. 4a). While no additional peaks appear on the heated PEDOT:PSS/perovskite substrates, additional peaks at 30.57° and 39.7° which belong to $PbBr_2$ are observed for NiO_x/perovskite substrates after heating at 150°C. Lowering the incident angle (2°) to detect the surface of the substrates indicate the absence of $PbBr_2$ peak, suggesting that $PbBr_2$ domains concentrate mostly at the bottom of the substrates. SEI and LABE images of the films after 150°C treatment indicate the growth of white domains from the NiO_x/perovskite interfaces (Supplementary Figs. 4b-c). This correlates to the white domains formed in the voltage biased NiO_x devices (Fig. 2).

In addition, no additional phase / domain formation (for example $NiBr_2$) is observed when NiO_x/MABr interface is heated up to 150°C (Supplementary Fig. 5). Hence, we associate the white domains detected in LABE to $PbBr_2$ rich perovskite domains. From these observations, we therefore conclude that NiO_x accelerates the creation of $PbBr_2$ rich domains upon voltage biasing while PEDOT/perovskite interface is more or less stable. This explains for the difference in switching property with both the interfaces.

This observation is in line with previous studies on NiO_x/$MAPbI_3$ interface where $Ni^{\geq 3+}$ defect sites may act as both a Lewis acid that oxidizes X^- anions and a Brønsted base that deprotonates the amine cations resulting in PbX_2 rich perovskite domains at the interface[34]. The applied external bias during memristor measurements are expected to lower the oxidation potentials and reaction barriers further. The appearance of the $PbBr_2$ rich domains upon bias application (Fig. 2**)** testifies this further. In conclusion, the NiO_x/perovskite interface reaction that promotes deprotonation of MABr and oxidation of Br^- anion could increase the number of ionic defects, increasing the probability of conductive filament formation in the system. In contrast, the more stable PEDOT:PSS/perovskite interfaces have less ionic defects upon external bias application which reduces the probability to form conductive filaments.

The hypothesis of conductive filament formation is further supported by the disappearance and reappearance of device capacitance after SET and RESET respectively for NiO_x devices (Supplementary Note 1, Supplementary Figures 6-7). For PEDOT:PSS devices, the formation of permanent conductive filaments is likely hampered by fewer halide vacancies in a more stable HTL/perovskite interface system. Although non-volatile memristive behaviour have been observed previously in halide perovskites with PEDOT:PSS as the HTL, most of them utilized reactive metals such as Al, Au, Ag, Cu, etc as the ETL which served as the ion source for conductive filament formation[35]. In summary, the ion permissive PEDOT:PSS interface promotes diffusive kinetics of ions in the perovskite, while the ion source NiO_x

interface supports drift kinetics and enables conductive filament formation, resulting in volatile diffusive and non-volatile drift memristive barristors respectively.

This ability to facilely tune the ionic drift and diffusive dynamics of halide perovskite memristive barristors paves way for an all-perovskite neuromorphic architecture with diffusive memristors employed as non-linear selectors and drift memristors as synaptic junctions- a matter for future research. In this work, we fashion the diffusive and drift memristors as artificial nociceptors and synapses to enable event-driven sensory signal computing, in line with the growing interest in realizing artificial afferent nerves that bridge sensing elements with processing units[36–39]. In comparison to earlier reports, we demonstrate a unique 3-tier decentralized decision-making process fusing sensing elements, halide perovskite memristive barristors and CMOS neurons for intelligent robotics.

Diffusive Memristive Barristors (Al/POT2T/MAPbBr$_3$/PEDOT:PSS/ITO) as Nociceptors:

Fig. 3 illustrates the working principle of biological nociceptors and the analogous artificial nociceptor. In the human nervous system, nociceptors are special receptors of sensory neurons that recognize noxious stimuli such as mechanical stress, extreme temperatures and chemical molecules. Acting as threshold switches, these receptors detect noxious stimuli above a pre-set noxious threshold, warns the central nervous system via generation of action potentials and initiates motor responses to minimize potential damage[40]. In stark contrast to other sensory receptors such as sight, hearing, taste, smell and touch that decrease their sensitivity when exposed to external stimuli for a prolonged time, these nociceptors operate in three states- normal, relaxation and sensitized. In the normal state, these receptors do not adapt to the sensory stimuli ("no adaptation") and hence maintains the same pain threshold over time. After arrival of a potentially noxious sensory stimulus, they enter an ultra-short term "relaxation" phase with enhanced sensitivity and latency to quickly respond to possible ensuing noxious stimuli. Highly intense noxious stimuli increases their sensitivity semi-permanently, finally resulting in "tissue damage" or "sensitization"[41]. In the injured or sensitized state, they recalibrate their threshold (decrease) and response (increase) to overprotect the injured site, thereby reducing the latency of emergency response. This phenomena of decreasing the pain threshold and increasing the response are called "allodynia" and "hyperalgesia" respectively[42]. In short, from a signal processing perspective, nociceptors filter significant noxious information from other sensory inputs exploiting the temporal correlations between noxious stimuli. The short-term memory features of relaxation and sensitization facilitates a preliminary or lower-order processing of sensory signals via thresholding.

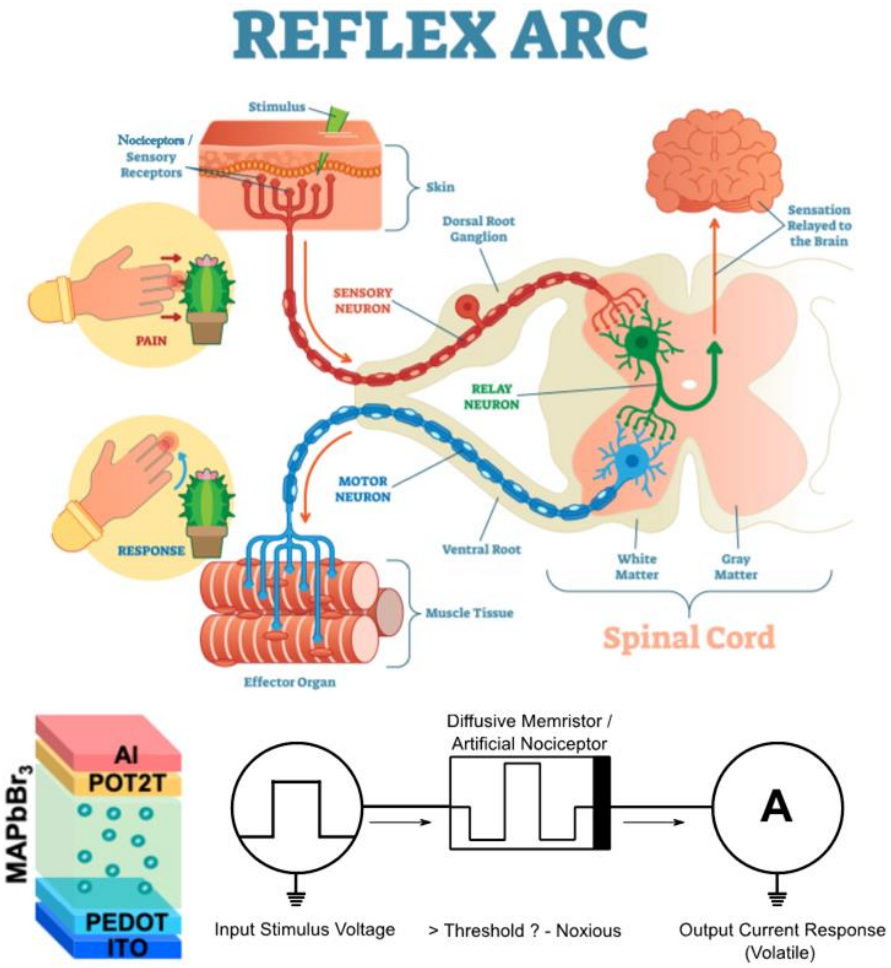

Fig 3. Nociceptive Signal Processing. Working principle of biological nociceptors and the analogous diffusive barristors as artificial nociceptors. Upon arrival of noxious stimuli, the nociceptor generates and relays action potentials to the central nervous system for signal processing. Similarly, voltage pulses applied to the diffusive HP memristors generate significant current outputs above the turn on voltage of the barristor.

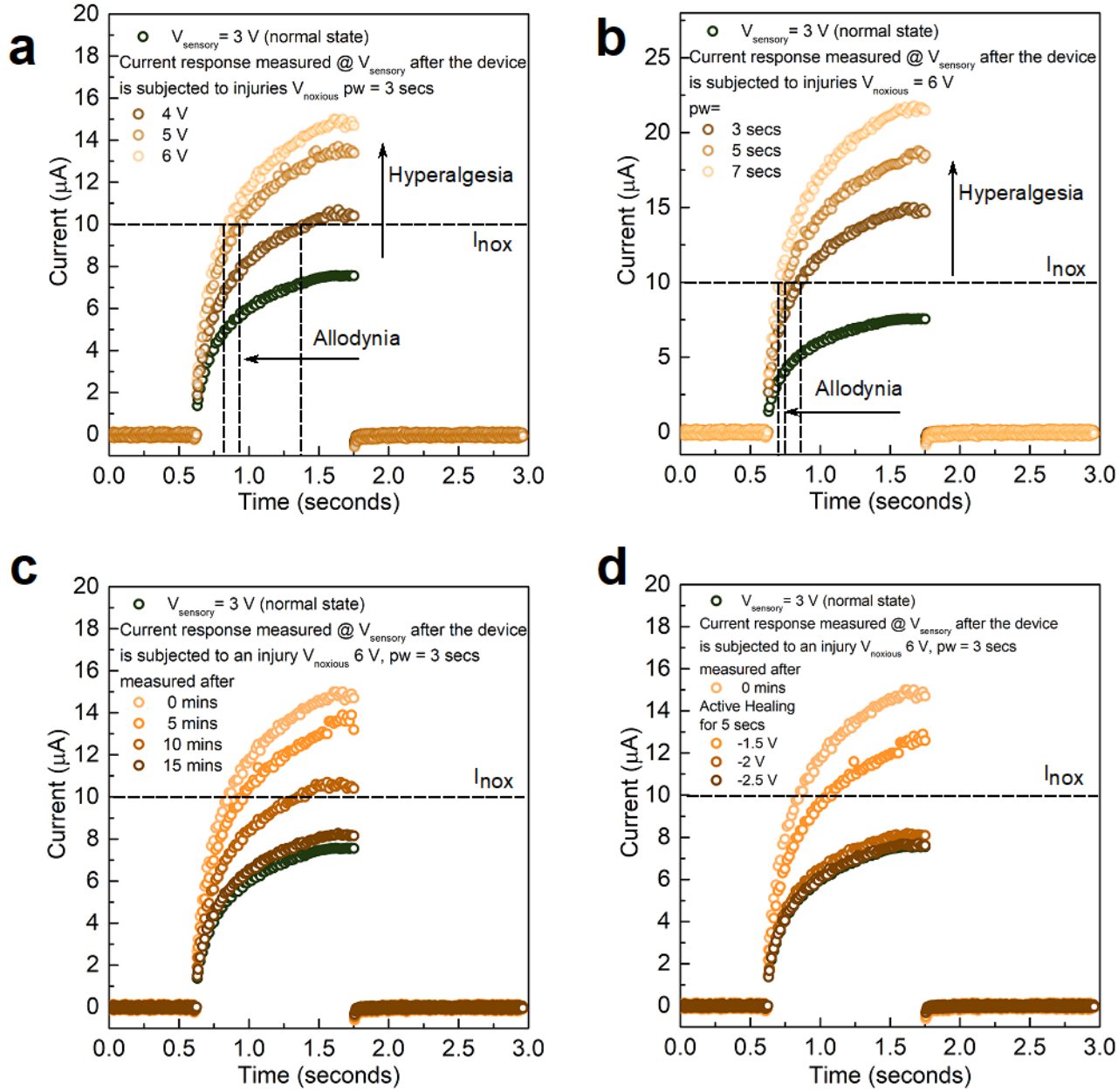

Fig 4. Nociceptive Signal Processing in Halide Perovskite (HP) Diffusive Memristors. a-d Sensory inputs of mild amplitude ($V_{sensory}$= 3 V) generate normal-state responses, while intense voltage shocks of high amplitude ($V_{noxious} \geq$ 4 V) generate sensitized responses. Normal-state responses are initially read at $V_{sensory}$= 3 V. The devices are next subjected to noxious stimuli, after which the sensitized responses are measured once again at $V_{sensory}$= 3 V. **a** Increased amplitude (4 V, 5 V and 6 V, pulse width = 3 s) and **b** pulse width (3, 5 and 7 secs, amplitude = 6 V) of the noxious stimuli enhance the current response and reduce the incubation time/threshold, akin to hyperalgesia and allodynia in biology. The diffusive threshold switching behaviour enables **c** passive healing with time and **d** active healing with curing pulses of opposite polarity. For **c**, the device is subjected to an injury of 6 V, pulse width = 3 secs. The responses are measured post-injury at $V_{sensory}$= 3 V after waiting for 5, 10 and 15 minutes respectively. For **d**, the device is subjected to an injury of 6 V, pulse width = 3 secs. Next, active healing pulses of -1.5, -2 and -2.5 V are applied for 5 secs and the responses are measured post-healing at $V_{sensory}$= 3 V.

In the perovskite nociceptor (Al/POT2T/$MAPbBr_3$/PEDOT:PSS/ITO), electrical voltage spikes mimic the sensory stimuli and induce volatile/threshold switching of the diffusive memristor. In the normal state, spike trains of innocuous stimuli ($V_{sensory} \leq$ 3 V, pw= 16 ms) induce hysteresis in the nociceptor, but the

output responses do not cross the warning (I_{warn} = 8 μA) nor pain (I_{nox} = 10 μA) thresholds and the diffusive memristor quickly relaxes back to its original state and gets ready to respond to the next stimulus. Persistent arrival of innocuous stimuli results in a unique saturation of the nociceptor response, a signature referred to as "no adaptation" (Supplementary Note 2, Supplementary Figure 8). This feature allows nociceptors to maintain the same warning and pain thresholds in the normal operation mode. Arrival of noxious-like a.k.a. warning stimuli (V_{warn} = 4 V, pw ≥ 1.5 s) causes threshold switching of the nociceptor, and the nociceptor outputs responses above the warning (I_{warn} = 8 μA) threshold to warn the system of possible ensuing noxious stimuli. The nociceptor enters the "relaxation" phase or alarmed state during which it recalibrates (increases) its sensitivity for a short-while to cater to the often repeated nature of such stimuli, but soon returns to its normal-state if noxious stimuli do not follow immediately. For e.g., innocuous stimuli ($V_{sensory}$ ≤ 3 V, pw = 16 ms) closely following (interval ≤ 20 ms) the warning stimuli (V_{warn} = 4 V, 1.5 s ≤ pw > 3 s) generates responses above the warning (I_{warn}= 8 μA) threshold and sustains the system in the alarmed state, while innocuous stimuli arriving after the relaxation interval (≥ 20 ms) generates insignificant responses below the warning threshold, bringing the system back to its normal-state (Supplementary Note 2, Supplementary Figure 9).

Intense voltage shocks representing injury ($V_{noxious}$≥ 4 V, pw ≥ 3 s) pushes the nociceptors to a "sensitized" phase or emergency state with enhanced sensitivity and latency to overprotect the injured site. To demonstrate "sensitization", the normal-state responses are initially measured with sensory stimuli ($V_{sensory}$= 3 V). Noxious stimuli or injury pulses ($V_{noxious}$≥ 4 V, pw ≥ 3 s) are next applied to the nociceptors, after which the sensitized current responses are measured at $V_{sensory}$= 3 V. Fig. 4 depicts the output responses before and after application of noxious stimuli. The responses now consistently cross the pain threshold (I_{nox}= 10 μA) to indicate severity of the injury, analogous to the increased firing rates of biological nociceptors. The nociceptors reduce their pain threshold, generating noxious action potentials to previously innocuous stimuli- a phenomenon called "allodynia"; and increase their response to normally innocuous stimuli (called "hyperalgesia"). Higher amplitudes (Fig. 4a, Supplementary Note 2, Supplementary Figure 10a) and pulse widths (Fig. 4b, Supplementary Note 2, Supplementary Figure 10b) of the noxious stimuli representing increasing severity of injuries decrease the incubation time (time taken to cross the pain threshold I_{nox}= 10 μA) further, reiterating the dosage-dependent threshold-switching behaviour of the nociceptors. Detailed electrical characterizations reveal increased baseline currents upon injury, implying a semi-permanent change in the device conductance, possibly because of the continuously diminishing hole injection barrier at the HP-PEDOT:PSS interface due to increased self p-doping. The injured states can spontaneously relax back to their resting state with time as shown in Fig. 4c, Supplementary Note 2, Supplementary Figure 10c, resembling the "passive self-healing" process of damaged biological tissues. More importantly, the injured states can be "actively healed/recovered" by applying "curing" pulses of opposite polarity (Fig. 4d, Supplementary Note 2, Supplementary Figure 10d). To further decouple film

thickness related effects and device-to-device variations, additional studies are conducted as a function of the thickness of the halide perovskite active layer and the variation of warning and pain thresholds among 25 devices are presented in Supplementary Note 2, Supplementary Figures 11-12.

From a device mechanism perspective, "hyperalgesia" and "allodynia" could be attributed to the self p- and n-doping effects within the halide perovskite layer and doping of the interlayers via ion diffusion in the memristive barristors. The passive healing process points to the back diffusion of ions within the halide perovskite layer due to the built-in potential of the barristor, while the active healing process could be attributed to the redistribution of ions in the halide perovskite layer and modification of the interfacial barriers with the opposite bias. Hence, the HP nociceptors comprehensively emulate all the signatures of their biological counterparts namely- "no adaptation", "relaxation" and "sensitization", by exploiting the ion migration, diffusion and relaxation effects at the perovskite-transport layer interfaces. In comparison, CMOS-based implementation of a single nociceptor would require 6 transistors and 1 capacitor to implement its adaptability to repeated noxious stimuli[13].

While nociceptors pre-process the signals via volatile threshold functions, learning of more complex phenomena like association entails memristive devices capable of being programmed to desired conductance states in a non-volatile manner. This weight plasticity forms the basis of all artificial neural networks (ANNs). Inspired from the adaptive strengthening and weakening of biological synapses, we next configure drift memristors based on Al/PO-T2T/$MAPbBr_3$/NiO_x/ITO as artificial synapses (ASs) to tackle higher-order learning features such as association and classical conditioning.

Drift Memristive Barristors (Al/POT2T/$MAPbBr_3$/NiO_x/ITO) as Synapses:

In neuroscience, synaptic plasticity is the ability of synapses to strengthen or weaken over time, in turn altering the interconnections between neural circuits in the brain. This forms one of the most important neurochemical foundations of learning and memory in biology, and is also a fundamental concept in the design of bio-inspired ANN architectures. Fig. 5a illustrates the working principle of biological synapses and the analogous artificial synapse. As a first evaluation of the conductance updates of weighted synaptic connections in an ANN, we investigate the analog programming window of HP synapses. As supposed to the DC bias scheme which results in a binary digital switching logic (Fig. 1b), spike-based write and erase operations without any compliance current control are adopted to identify stable intermediate resistance states and efficiently map the analog and digital switching regimes. Since these devices would finally be utilized as weighted synaptic connections in a bio-inspired spiking neural network operating based on temporal correlations between input spike trains, this pulsed/AC mode of evaluation is further justified. To evaluate the soft bounded nature of the cumulative conductance change[43], i.e., mapping of the voltage window where the HP synapses portray non-abrupt weight updates, absolute weights are programmed to a

common initial conductance and weight changes produced by 40 identical write/erase pulses are traced. Input pulses of amplitude +3 V to +6 V maps the potentiation window, while -3 V to -6 V records the depression window. The drift memristive barristors demonstrate multilevel conductance programmability with high voltage dependence. No significant switching is observed for potentiation operations below the threshold of + 3.5 V. Higher voltages between + 4 V to + 5.5 V exhibit more gradual and analog increments, subsequently approaching a plateau or soft conductance boundary (Fig. 5b). Programming voltages higher than + 5.5 V result in abrupt conductance updates and exhibit a digital switching characteristic, indicating the trade-off between analog weight updates and dynamic range. In short, the switching transitions in the potentiation window can be classified into three different operating regimes as 'no switching'- < 3.5 V, + 4 V $\leq$ 'gradual analog switching' $\geq$ + 5.5 V and 'digital deterministic switching' > + 5.5 V. From a mechanistic perspective, the evolution of such regimes can be explained by the transition of kinetics in filament formation with stimuli intensity. Although a large stimulus would be able to produce a wider memory window, it is also expected to transit towards a digital bi-stable operation. Such digital operations have little use as synaptic connections utilized to store analog weights. Therefore, the trade-off between conductance window and analog programmability requires the optimization of programming pulse voltages for synaptic operations. To understand the evolution of the potentiation operations further, the conductance changes are mapped as a function of the absolute conductance levels and programming voltages (Fig. 5c). Weight updates corresponding to + 3.5 V result in a negligible localized window and is hence classified as 'no switching'. 'Gradual analog switching' observed in the range of + 4 to + 5.5 V leads to multiple distributed conductance states across the memory window. As programming voltages are increased further, the switching approaches a 'digital deterministic switching' characteristic with larger conductance updates but less distributed states. This deterministic behavior is akin to a conventional bi-stable memristor, undesirable for multi-bit synaptic operations.

To account for the analog programming window, we employ a 2-parameter multiplicative update model to capture further insights[44]. For normalized synaptic weights denoted between 0 and 1, the following generalized soft bound equations are adopted for incremental and decremental weight changes in potentiation and depression events, respectively.

$$\delta w_{+}(w) = \alpha\,(1- w)^{\gamma} \qquad (1)$$

$$\delta w_{-}(w) = \alpha\, w^{\gamma} \qquad (2)$$

where α is a multiplicative parameter which indicates the magnitude of weight modification and γ reflects the nature of boundary approach of the weight update. The parameters α and γ extracted from the normalized weights are shown in Fig. 5d. Programming voltages $\leq$ + 3.5 V produce negligible weight changes and depict a highly confined memory window. In the analog regime (+ 4 V to + 5.5 V), the

extracted parameters α and γ are compared in terms of their ideality factors. + 5 V as the potentiation voltage shows the smallest α and highest γ. A high α indicates an abrupt initial step with poor distribution across the conductance window, whereas a smaller α ensures more programmable conductance states with 1/α intervals. Similarly, a high γ indicates a stronger deviation from linearity, ensuring a more gradual increment towards the conductance boundaries at the expense of dynamic range. Although the programming voltage of + 5.5 V produces a larger memory window, + 5 V with a smaller α and higher γ portrays a wider analog window with gradual incremental weight updates, thus making it the optimal voltage for softly bounded analog operations. In this analysis, + 6 V pulses were also observed to exhibit analog programmability. However, since the achieved weights are close to the conductance limit of the device, continuous operation at + 6 V is avoided for synaptic operations.

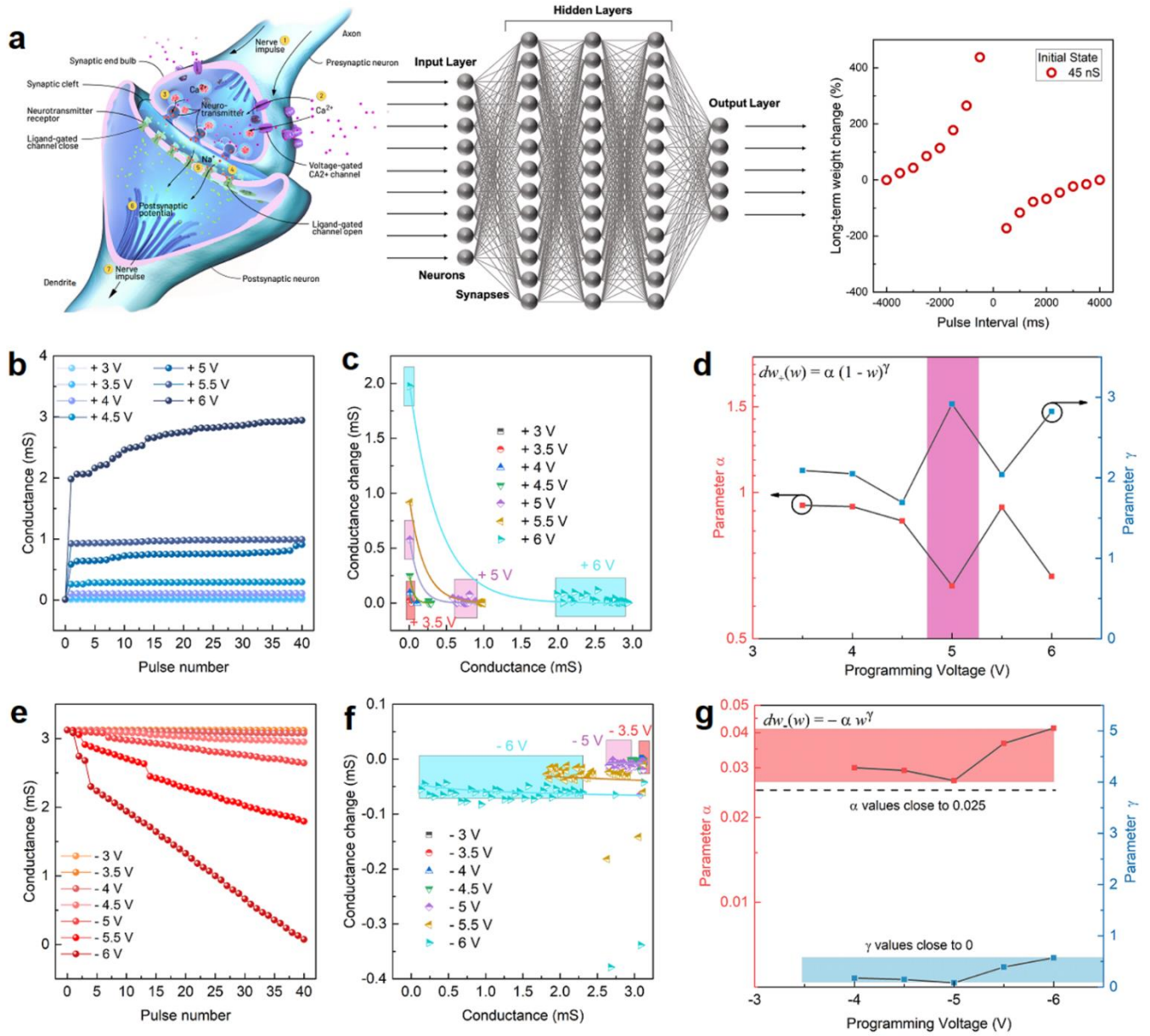

Fig 5. Halide perovskite drift memristive barristors as weighted synaptic connections. a Synaptic interconnections between neurons form the crux of the decision making process in both biological and artificial neural networks. The image on the right depicts the asymmetric anti-Hebbian spike-timing-dependent-plasticity (STDP) rule implemented in $MAPbBr_3$ drift memristive barristors. **Mapping the analog programming window. b** Conductance updates with identical set pulses. **c** Conductance

increments as a function of absolute conductance levels with potentiation operations. **d** Modelled with a soft conductance boundary limit, the conductance change can be described by two parameters- α and γ. The variation in multiplicative parameter α and state dependency factor γ with respect to programming voltage indicates the nature of weight updates during potentiation. **e-g** Conductance updates as a function of the number of reset pulses, absolute conductance levels and variation in multiplicative parameters modelled with a soft conductance boundary limit during depression respectively.

In contrast, the depression operations are governed by very different weight update dynamics. This can be explained by the asymmetry in the formation and rupturing of filaments in the potentiation and depression operations respectively. Depression operations produce highly linear weight updates as shown in Fig. 5e. This asymmetry is also reflected in the wider conductance distribution with similar programming amplitudes in Fig. 5f as compared to the potentiation operations in Fig. 5c. From Fig. 5f, the required threshold voltage of – 4 V (to produce at least 0.3 mS conductance change) is observably similar to the setting threshold of + 4 V. Furthermore, the conductance increments are modelled to be highly linear as shown in Fig. 5g. As a reference, a perfectly linear conductance update would have an $\alpha = 1/40 = 0.025$ with evenly distributed conductance updates and $\gamma = 0$ with no state dependence nor soft boundary. Although the depression operations are shown to be linear and incapable of approaching with a soft boundary in these measurements, we observe that the device still presents highly analog programmability (α close to 0.025) across the range of depression voltages (- 4 V to - 6 V). The disadvantage is that such linear operations would instead face a more abrupt transition (γ close to 0) towards a hard boundary (for example ~ 10 μS conductance). However, this can be avoided by further fine-tuning the programming pulses in terms of pulse amplitude, number, width and frequency. In summary, we expect to extract gradual weight updates from our HP memristive barristor across + 4 V to + 5.5 V for potentiation operations and - 4 V to - 6 V for depression. This indicates the limited window for true analog weight updates, ideal for ANNs. Input voltages below and above this cause insignificant/highly abrupt weight updates, undesirable for ANNs. From the design viewpoint of an artificial neural network (ANN), evaluation of the window for true analog weight updates is highly critical and can be generalized for a wide variety of memristive materials and devices.

Based on the analog programming window, we next benchmark the HP synapses on the spike-timing-dependent-plasticity (STDP) rule-a bio-plausible unsupervised learning mechanism that manipulates synaptic weights based on the temporal correlations between pre- and post-synaptic spike timings. In ANNs, the STDP rule is most commonly used in a layer-wise manner to train the convolutional kernels to enable them to self-learn (unsupervised) features from input spike patterns locally. To characterize this plasticity rule, spike patterns corresponding to those shown in Supplementary Note 3, Supplementary Figure 13 are applied to the pre- and post-synaptic terminals of the HP synapse, and the change in conductance (weight) is recorded as a function of the pulse interval between pre- and postsynaptic spikes. Temporal correlations between the pre- and postsynaptic spikes create voltage-dependent changes in

conductance/weight, establishing an asymmetric anti-Hebbian STDP rule - a causal temporal order of pre-synaptic activity followed by postsynaptic activity leads to long-term depression (LTD) while the reverse order leads to long-term potentiation (LTP) (Fig. 5a, Supplementary Note 3, Supplementary Figure 14). It is important to note that the synapses depict smooth analog weight updates when the effective voltage developed across the device lies within the analog programming window, while abrupt weight updates are observed when this condition is violated. In line with the observations in Figs. 5b-f, a state-dependence is observed for the STDP behavior, i.e. the weight update trace can be modulated as a function of the absolute initial conductance level (Supplementary Note 3, Supplementary Figure 14). Often overlooked in most investigations, these results provide a sound guideline to extract analog weight updates from memristive devices and can be adopted as a universal approach for analyzing new memristive materials and devices as artificial synapses.

Robot Integration

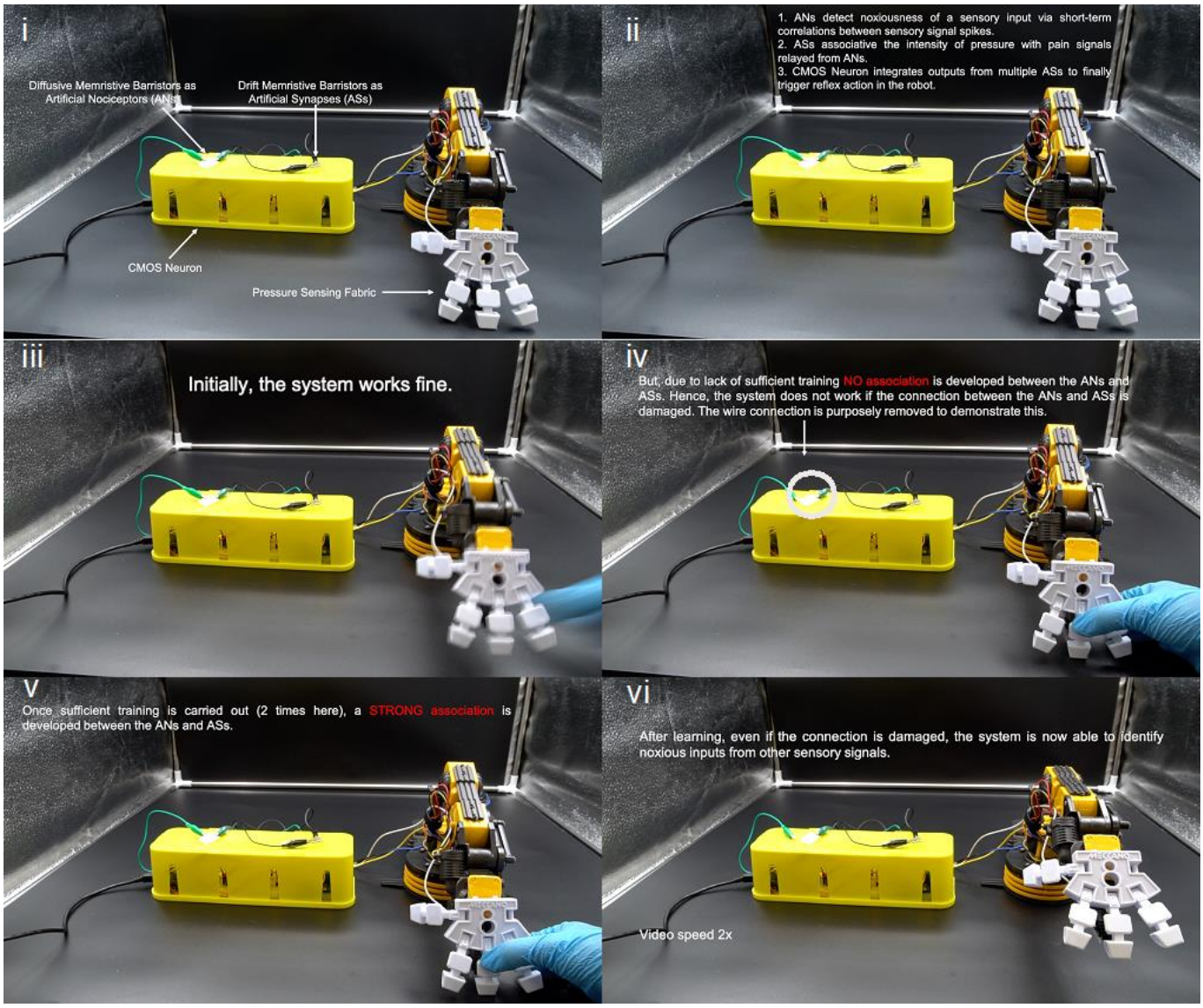

Fig 6. Demonstration of the decentralized learning enabled by halide perovskite neuromorphic elements for effficient sensory signal computing. Associative learning of pain and pressure signals using pressure sensing fabrics, diffusive memristive

barristors as artificial nociceptors, drift memristive barristors as artificial synapses and a CMOS neuron. (i-vi) shows a sensorimotor robotic platform capable of detecting and associating noxious pressure stimuli in real time.

Finally, we integrate the HP nociceptors and synapses with a CMOS neuron (Supplementary Note 4, Supplementary Figures 15-17, Supplementary Table-1) and demonstrate a prototypical sensory signal computing platform that learns noxious sensory information and triggers reflex reactions on a sensorized robotic arm. By integrating these spike-based learners with sensing elements, we decentralize the decision-making to the location of the sensing nodes. This approach alleviates issues related to wiring, latency, fault tolerance and robustness- challenges for information processing in robotic skins[45]. In this approach, the decision making occurs at three stages- (i) nociceptors detect and learn nociceptive signal patterns, (ii) synapses establish correlations and association between other sensory modalities (e.g. texture) and nociceptive signals, and (iii) the CMOS neuron integrates multiple synaptic weights[13].

We first demonstrate this decision making process tangibly via conductance measurements during training and inference (Supplementary Note 4, Supplementary Figure 18). Sensory signals are converted to simple spike trains for convenient analysis. Noxious sensory signals are represented by “101001”, while non-noxious signals are represented by “100100”, “011000”, “111000”, “101100”, “001110”, “101010” and “001101”. After four training repetitions with noxious sensory signals, a strong association is developed between the nociceptor and the six connected synapses, resulting in a significant total weight change (> 900 μS) corresponding to the noxious sensory signal. All other stimuli fail to cause significant weight changes and hence the system clearly distinguishes noxious information from other sensory inputs. The high degree of association developed between the nociceptor and synapses is reflected by the stability of the output response during the inference stage in the absence of the nociceptive input. In comparison to existing two-terminal oxide memristor implementations of artificial nociceptors and afferent nerves[12,36,38], this is the first demonstration of integration of associative learning between nociceptors and synapses, comprehensively illustrating the utility of nociceptive thresholds and synaptic association for event-driven sensory signal computing. This association also imparts fault-tolerance to the decision-making process- post training, the synapses can still correlate to noxious stimuli even if the nociceptors are damaged inadvertently. These synaptic outputs can be used to modulate the firing rates of a CMOS neuron, completing the decision making process.

As a final demonstration, we integrate all these elements and demonstrate a real-time intelligent sensory system capable of detecting noxious pressure stimuli such as pinching (Fig. 6 and Supplementary Movie 1). We specifically address pain perception and the association of nociception with pressure sensory perception to trigger escape reflex in a sensorized robotic arm. To complete the signalling pathway, we integrate pressure sensing fabrics with nociceptors and synapses fashioned as peripheral signal processors

and a CMOS neuron circuit to relay the signals. On arrival of a noxious pressure stimulus (e.g. pinching of the fabric integrated on to the fingers of the robotic arm), the perovskite nociceptors generate a high output response above the pain threshold in their sensitized state. The signals are relayed to perovskite synapses, resulting in non-volatile conductance updates in accordance to the severity of the injury. Weight changes to the synapses in turn increases the firing rate of the CMOS neuron circuit, triggering the robot's motion away from the source of potential damage, akin to motor responses in the human body.

Discussion

Most halide perovskite (HP) memristive implementations typically rely on electrochemical metallization reactions of a reactive electrode (e.g. Ag) in direct contact with the active perovskite switching matrix. This results in unavoidable metal-HP electrochemical reactions, often limiting the device reliability and endurance[46–48]. More critically, this approach almost always results in a highly abrupt switching behaviour (in both DC and pulsed/AC modes) and thus, limits the ability to tune the switching characteristics. Since neuromorphic computing requires devices with multiple programmable conductance states accessible in an analog manner, this inability to tune the switching characteristics can be a limiting factor. In contrast, we exploit the intimately coupled ionic-electronic charge transport unique to halide perovskites- specifically their intrinsic self-doping, and identify key interfaces that modulate the interfacial doping barriers. The organic ion permissive PEDOT:PSS interface promotes diffusive kinetics modulating the carrier injection barrier with the perovskite layer resulting in volatile diffusive threshold switching, while the ion source NiO_x interface supports drift kinetics and formation of conductive filaments resulting in non-volatile drift memristive switching. This ability to readily modulate the switching characteristics allows us to fashion these elements as artificial nociceptors and synapses, enabling sensory signal computing.

We report the first diffusive halide perovskite (HP) memristor and artificial nociceptor to the best of our knowledge. The intrinsic migration of ions dopes and dedopes the PEDOT:PSS interface facilely to enforce volatile thresholding functions such as "relaxation", "sensitization" and "no adaptation". Compared to oxide diffusive memristors which rely on a reservoir of reactive electrode atoms (e.g. Ag), defect engineering of trap energy levels and electrode work functions to achieve these characteristics[12,49], our results prove the feasibility of utilizing the intrinsic migration and back-diffusion of ions and vacancies unique to HPs, as a proxy to achieve the same. On the other hand, the ion source NiO_x interface supports formation of conductive filaments via drift of halogen vacancies in the perovskite layer and oxygen vacancies in the NiO_x layer resulting in programmable artificial synapses. On benchmarking the digital memory performance, our NiO_x-based memristors compare favourably to state-of-the-art in halide perovskites (Supplementary Note 5, Supplementary Figure 19). In comparison to the existing implementations of halide perovskite synapses that fail to map out the analog programming window, we report the first comprehensive analysis of the soft boundaries of conductance updates these devices- a

crucial design requirement for ANNs. This is also the first analysis of its kind on an organic memristive material system to the best of our knowledge and can be extended to a wide variety of memristive materials and devices, providing a comprehensive guideline for analog programming of weighted synaptic connections. This allows us to optimize input spike trains to limit the synapse's operation to within the analog programming window, hence enabling state-dependent spike-timing-dependent-plasticity (STDP) local learning rules, comprehensively qualifying halide perovskite drift memristors as weighted synaptic connections for neuromorphic computing.

Finally as a demonstrator, we present a novel decentralized sensory signal processing prototype targeted at intelligent robotics- relaxation and sensitization of artificial nociceptors helps learn the severity of noxious stimuli based on temporal correlations [first stage]; artificial synapses learn high-order correlations (e.g. texture) from the sensory signals via classical conditioning/associative learning [second stage]; and the CMOS neuron integrates synaptic weights [third stage], facilitating localised decision making. This approach helps embed intelligence within the sensor nodes, alleviating challenges related to wiring, latency and fault tolerance- major bottlenecks for sensory signals processing in robotics. When compared to conventional CMOS technology, these novel devices enable in-memory computing at the sensor node with much simpler circuitry. This decentralized approach with halide perovskite memristive devices is the first of its kind and pushes intelligence to the edge, facilitating the fusion of sensory data with bio-inspired learning algorithms. Unlike the very recent artificial afferent nerve implementations with organic synaptic transistors[39] and Mott memristors[36], the proposed system incorporates learning and decision making at the sensor node. The prototypical memristive platform composed of halide perovskite artificial nociceptors, synapses and CMOS neuron, although simple, is the first of its kind, serves as a proof-of-concept demonstration and represents a significant advance for halide perovskites and ionotronic memristive materials, paving way for implementations fusing new organic electrochemical material systems, memristor technology and robotics.

Experimental:

Devices fabrication: Indium doped tin oxide (ITO, 7 $\Omega.cm^{-2}$) coated glass substrates were cleaned by sequential sonication in decon soap, distilled water, and isopropanol solution. Substrates were dried and exposed to oxygen plasma for 15 min. Two types of HTL were fabricated, i.e. NiO_x and PEDOT:PSS. To deposit NiO_x layer, equimolar solution (0.5M) of nickel nitrate hexahydrate and ethylene diamine in ethylene glycol solvent was spun coated (6000 rpm for 60 s), followed by annealing at 300°C for 1 hour in ambient atmosphere. PEDOT:PSS films were deposited by spin-coating (4000 rpm for 60s) the precursors (Clevios, Al 4083) and followed by annealing at 150°C for 15 minutes. Films were then transported into argon filled glovebox for perovskite deposition. Equimolar (1M) $PbBr_2$ and CH_3NH_3Br in mixed DMF/DMSO solvent (3:1) were used as the perovskite precursors. Perovskite films were deposited via spin

coating (5000 rpm for 30s) and an anti-solvent (toluene) was introduced 5 s after the spinning start to promote fast nucleations. Approximately 40 nm of ((1,3,5-triazine-2,4,6-triyl)tris(benzene-3,1-diyl))tris(diphenylphosphine oxide) (POT2T), 1 nm LiF, and 100 nm Al were thermally evaporated in sequence to complete the device fabrication. Shadow masks with active area of $8mm^2$ were used during electrode deposition. Devices were then encapsulated inside glovebox and tested in ambient atmosphere.

Characterizations: Bruker D8 advance diffractometer with 0D LynxEYE^{TM} detector was used to record the X-Ray Diffraction (XRD) pattern of the films. Field effect scanning electron microscope (FE-SEM, JEOL J7600F) were utilized to capture the topographical and cross sectional images. Absorption and steady state PL spectra were collected using Shimadzu UV-3600 UV-Vis-NIR spectrophotometer and Horiba Fluoromax-4 respectively. Impedance measurements were carried out using Autolab 302N. Ultraviolet Photoelectron Spectroscopy (UPS, Kratos AXIS Supra) with He plasma at excitation energy of 21.22 eV was used to probe the valence band and work function position of the materials.

Acknowledgements. This research was funded by Singapore Ministry of Education-Tier 2 Grants-MOE2016-T2-1-100 and MOE2018-T2-2-083 and National Research Foundation, Prime Minister's Office, Singapore under its Competitive Research Programme (CRP Award No. NRF-CRP14-2014-03) and the Intra-CREATE Collaborative Grant (NRF2018-ITC001-001) .

Author contributions. R.A.J., A.B. and N.M. conceived the experiments. R.A.J. performed all the optoelectronic characterizations along with N.Y. and S.E.N. under the supervision of N.M.. N.Y. and N.F.J. fabricated the barristors under the supervision of N.M. and S.G.M.. N.Y. performed all the electron microscopy experiments under the supervision of N.M. and S.G.M.. S.E.N. analysed the analog programming window for the drift memristors, collected device statistics and measured the switching speed of the drift memristors along with M.R.K.. M.I.B.P., M.R.K. and A. programmed the arduino controller and set up the final robot demonstration. J.B. designed the LIF neuron circuit under the supervision of A.B.. R.A.J., N.Y., S.E.N., A.B. and N.M. wrote the manuscript with comments from all authors.

Competing interests. The authors declare no competing interests.

Additional information. Supplementary Information accompanies this paper.

Data availability. The data that support the findings of this study are available from the corresponding author upon reasonable request.

Supplementary Materials. Supplementary Text, Supplementary Figures: 1-19, Supplementary Table-1, Supplementary Movie 1

References:

[1] M. A. Zidan, J. P. Strachan, W. D. Lu, *Nat. Electron.* **2018**, *1*, 22.

[2] A. Sebastian, M. Le Gallo, R. Khaddam-Aljameh, E. Eleftheriou, *Nat. Nanotechnol.* **2020**, 1.

[3] R. A. John, J. Acharya, C. Zhu, A. Surendran, S. K. Bose, A. Chaturvedi, N. Tiwari, Y. Gao, Y. He, K. K. Zhang, *Nat. Commun.* **2020**, *11*, 1.

[4] Y. van de Burgt, E. Lubberman, E. J. Fuller, S. T. Keene, G. C. Faria, S. Agarwal, M. J. Marinella, A. A. Talin, A. Salleo, *Nat. Mater.* **2017**, *16*, 414.

[5] E. J. Fuller, S. T. Keene, A. Melianas, Z. Wang, S. Agarwal, Y. Li, Y. Tuchman, C. D. James, M. J. Marinella, J. J. Yang, *Science (80-.).* **2019**, *364*, 570.

[6] Y. Lee, T.-W. Lee, *Acc. Chem. Res.* **2019**, *52*, 964.

[7] Y. van De Burgt, A. Melianas, S. T. Keene, G. Malliaras, A. Salleo, *Nat. Electron.* **2018**, *1*, 386.

[8] Y. Tuchman, T. N. Mangoma, P. Gkoupidenis, Y. van de Burgt, R. A. John, N. Mathews, S. E. Shaheen, R. Daly, G. G. Malliaras, A. Salleo, *MRS Bull.* **2020**, *45*, 619.

[9] Q. Xia, J. J. Yang, *Nat. Mater.* **2019**, *18*, 309.

[10] Z. Wang, S. Joshi, S. E. Savel'ev, H. Jiang, R. Midya, P. Lin, M. Hu, N. Ge, J. P. Strachan, Z. Li, *Nat. Mater.* **2017**, *16*, 101.

[11] R. Midya, Z. Wang, S. Asapu, X. Zhang, M. Rao, W. Song, Y. Zhuo, N. Upadhyay, Q. Xia, J. J. Yang, *Adv. Intell. Syst.* **2019**, *1*, 1900084.

[12] J. H. Yoon, Z. Wang, K. M. Kim, H. Wu, V. Ravichandran, Q. Xia, C. S. Hwang, J. J. Yang, *Nat. Commun.* **2018**, *9*, 417.

[13] R. A. John, N. Tiwari, M. I. Bin Patdillah, M. R. Kulkarni, N. Tiwari, J. Basu, S. K. Bose, Ankit, C. J. Yu, A. Nirmal, S. K. Vishwanath, C. Bartolozzi, A. Basu, N. Mathews, *Nat. Commun.* **2020**, *11*, 4030.

[14] N. K. Upadhyay, H. Jiang, Z. Wang, S. Asapu, Q. Xia, J. Joshua Yang, *Adv. Mater. Technol.* **2019**, *4*, 1800589.

[15] R. Dittmann, J. P. Strachan, *APL Mater.* **2019**, *7*, 110903.

[16] R. A. John, N. Yantara, Y. F. Ng, G. Narasimman, E. Mosconi, D. Meggiolaro, M. R. Kulkarni, P. K. Gopalakrishnan, C. A. Nguyen, F. De Angelis, *Adv. Mater.* **2018**, 1805454.

[17] P. C. Harikesh, B. Wu, B. Ghosh, R. A. John, S. Lie, K. Thirumal, L. H. Wong, T. C. Sum, S. Mhaisalkar, N. Mathews, *Adv. Mater.* **2018**, *30*, 1802080.

[18] P. C. Harikesh, A. Surendran, B. Ghosh, R. A. John, A. Moorthy, N. Yantara, T. Salim, K. Thirumal, W. L. Leong, S. Mhaisalkar, *Adv. Mater.* **2020**, 1906976.

[19] W. Tress, *J. Phys. Chem. Lett.* **2017**, *8*, 3106.

[20] X. Zhu, Q. Wang, W. D. Lu, *Nat. Commun.* **2020**, *11*, 1.

[21] S. Lee, H. Kim, D. H. Kim, W. Bin Kim, J. M. Lee, J. Choi, H. Shin, G. S. Han, H. W. Jang, H. S. Jung, *ACS Appl. Mater. Interfaces* **2020**, *12*, 17039.

[22] S. G. Kim, Q. Van Le, J. S. Han, H. Kim, M. Choi, S. A. Lee, T. L. Kim, S. B. Kim, S. Y. Kim, H. W. Jang, *Adv. Funct. Mater.* **2019**, *29*, 1906686.

[23] S. Kim, J. Yang, E. Choi, N. Park, *Adv. Funct. Mater.* **2020**, 2002653.

[24] X. Guan, W. Hu, M. A. Haque, N. Wei, Z. Liu, A. Chen, T. Wu, *Adv. Funct. Mater.* **2018**, *28*, 1704665.

[25] P. C. Harikesh, B. Febriansyah, R. A. John, N. Mathews, *MRS Bull.* **2020**, *45*, 641.

[26] A. Jaffe, Y. Lin, C. M. Beavers, J. Voss, W. L. Mao, H. I. Karunadasa, *ACS Cent. Sci.* **2016**, DOI 10.1021/acscentsci.6b00055.

[27] M. Saba, M. Cadelano, D. Marongiu, F. Chen, V. Sarritzu, N. Sestu, C. Figus, M. Aresti, R. Piras, A. G. Lehmann, *Nat. Commun.* **2014**, *5*, 1.

[28] C. Eames, J. M. Frost, P. R. F. Barnes, B. C. O'regan, A. Walsh, M. S. Islam, *Nat. Commun.* **2015**, *6*, 1.

[29] K. Domanski, B. Roose, T. Matsui, M. Saliba, S.-H. Turren-Cruz, J.-P. Correa-Baena, C. Roldán Carmona, G. Richardson, J. M. Foster, F. De Angelis, J. M. Ball, A. Petrozza, N. Mine, M. K. Nazeeruddin, W. Tress, M. Grätzel, U. Steiner, A. Hagfeldt, A. Abate, *Energy Environ. Sci.* **2017**, *10*, 604.

[30] P. Calado, A. M. Telford, D. Bryant, X. Li, J. Nelson, B. C. O'Regan, P. R. F. Barnes, *Nat. Commun.* **2016**, 1.

[31] Y. Luo, P. Khoram, S. Brittman, Z. Zhu, B. Lai, S. P. Ong, E. C. Garnett, D. P. Fenning, *Adv. Mater.* **2017**, *29*, 1.

[32] X. Zhao, H. Xu, Z. Wang, Y. Lin, Y. Liu, *InfoMat* **2019**, inf2.12012.

[33] D. Di Girolamo, F. Matteocci, F. U. Kosasih, G. Chistiakova, W. Zuo, G. Divitini, L. Korte, C. Ducati, A. Di Carlo, D. Dini, A. Abate, *Adv. Energy Mater.* **2019**, *9*, DOI 10.1002/aenm.201901642.

[34] C. C. Boyd, R. C. Shallcross, T. Moot, R. Kerner, L. Bertoluzzi, A. Onno, S. Kavadiya, C. Chosy, E. J. Wolf, J. Werner, J. A. Raiford, C. de Paula, A. F. Palmstrom, Z. J. Yu, J. J. Berry, S. F. Bent, Z. C. Holman, J. M. Luther, E. L. Ratcliff, N. R. Armstrong, M. D. McGehee, *Joule* **2020**, *4*, 1759.

[35] X. Xiao, J. Hu, S. Tang, K. Yan, B. Gao, H. Chen, D. Zou, *Adv. Mater. Technol.* **2020**, *5*, 1.

[36] X. Zhang, Y. Zhuo, Q. Luo, Z. Wu, R. Midya, Z. Wang, W. Song, R. Wang, N. K. Upadhyay, Y. Fang, *Nat. Commun.* **2020**, *11*, 1.

[37] X. Liao, W. Song, X. Zhang, C. Yan, T. Li, H. Ren, C. Liu, Y. Wang, Y. Zheng, *Nat. Commun.* **2020**, *11*, 1.

[38] H. Tan, Q. Tao, I. Pande, S. Majumdar, F. Liu, Y. Zhou, P. O. Å. Persson, J. Rosen, S. van Dijken,

Nat. Commun. **2020**, *11*, 1.

[39] Y. Kim, A. Chortos, W. Xu, Y. Liu, J. Y. Oh, D. Son, J. Kang, A. M. Foudeh, C. Zhu, Y. Lee, *Science (80-.).* **2018**, *360*, 998.

[40] A. E. Dubin, A. Patapoutian, *J. Clin. Invest.* **2010**, *120*, 3760.

[41] J. L. Rhudy, E. J. Bartley, A. E. Williams, *Pain* **2010**, *148*, 320.

[42] J. Sandkuhler, *Physiol. Rev.* **2009**, *89*, 707.

[43] J. Frascaroli, S. Brivio, E. Covi, S. Spiga, *Sci. Rep.* **2018**, *8*, 7178.

[44] S. Fusi, L. F. Abbott, *Nat. Neurosci.* **2007**, *10*, 485.

[45] G. Cheng, E. Dean-Leon, F. Bergner, J. R. G. Olvera, Q. Leboutet, P. Mittendorfer, *Proc. IEEE* **2019**, *107*, 2034.

[46] Q. Lin, W. Hu, Z. Zang, M. Zhou, J. Du, M. Wang, S. Han, X. Tang, *Adv. Electron. Mater.* **2018**, *4*, 1700596.

[47] S. Ge, Y. Huang, X. Chen, X. Zhang, Z. Xiang, R. Zhang, W. Li, Y. Cui, *Adv. Mater. Interfaces* **2019**, *6*, 1802071.

[48] C. Zou, L. He, L. Y. Lin, *Phys. status solidi (RRL)–Rapid Res. Lett.* **2019**, 1900182.

[49] Y. Kim, Y. J. Kwon, D. E. Kwon, K. J. Yoon, J. H. Yoon, S. Yoo, H. J. Kim, T. H. Park, J. Han, K. M. Kim, *Adv. Mater.* **2018**, *30*, 1704320.